DESCRIPTION OF MATHEMATICAL MODEL OF INTERACTIONS BETWEEN AUXIN AND PIN1

We have considered two representations of a longitudinal section of the shoot apex: a regular grid and a cellular template based on a real meristem section. Depending on the case, cells are represented as square or arbitrary polygons, which share with the neighboring cells the edges that represent the interface through which the cells communicate. Each edge thus corresponds to a pair of membranes with the associated wall. The model equations take into account the variation in cell and interface size present in the cellular template model. Our model treats cells as single compartments and does not explicitly simulate internal auxin gradients within a cell or the diffusion of auxin in the extracellular space. In the shoot meristem, where the cells are small and have thin walls, this is likely a reasonable approximation (Kramer 2006). In a review of computer models of auxin transport, Kramer (Kramer 2008) discusses the strengths and weaknesses of this and other approaches.

Based on assumptions 1-5 in the main text, a set of coupled ordinary differential equations is used to model the production and decay of auxin (IAA) and PIN1 proteins, as well as the diffusion and transport of IAA. Numerical integration is performed using the forward Euler method. At the beginning of each simulation time step, all PIN1 proteins in each cell are allocated to cell membrane sections based on a combination of the flux across the interface and the concentration of auxin in the neighboring cells. It is assumed that relocalization of PIN1 is fast compared to the length of the simulation step, and therefore the system operates in a quasi steady-state with respect to PIN1 allocation.

The change in the total amount of PIN contained in a cell is given by

$$\frac{d\,PIN_i}{dt} = \frac{\rho_{PIN_0} + \rho_{PIN} IAA_i}{1 + \kappa_{PIN} PIN_i} - \mu_{PIN} PIN_i \,, \tag{1}$$

where PIN_i and IAA_i are the concentrations of PIN1 and IAA in cell i, ρ_{PIN_0} controls auxin-independent PIN1 production, ρ_{PIN} controls PIN1 production based on IAA concentration, κ_{PIN} is a coefficient limiting PIN1 production, and μ_{PIN} controls decay of PIN1. There is no auxin-independent PIN1 production in the inner cells, and thus PIN1 production in these cells is entirely dependent on IAA concentration.

We assume reduced communication between the L1 layer and inner tissue that is considered when calculating transport, diffusion, and PIN1 orientation involving interfaces that cross this boundary. This reduction factor, $B_{(i,j)}$, is given as a model parameter and is set to 1 if the cells are of the same type.

Allocation of PIN1 to sections of the plasma membrane depends both on the concentration of IAA in neighbor cells and the IAA flux across the interface. In

canalization models (Mitchison 1980b; Mitchison 1981; Feugier et al. 2005; Rolland-Lagan and Prusinkiewicz 2005; Feugier and Iwasa 2006), carriers allocated to cell membranes accumulated over many time steps, whereas in the transport-based phyllotaxis models (Jonsson et al. 2006; Smith et al. 2006), all of the carriers in a cell were allocated to the membrane at each time step. In order to combine models, we introduce a variable $F_{i\to j}$, associated with each interface between cells, which reflects the flux history across this interface. The change in this variable for the section of membrane in cell *i* facing cell *j* is given by

$$\frac{d\,F_{i\to j}}{dt} = B_{(i,j)} \cdot \frac{\rho_{F_0} + \rho_F \max^2\left(0, \phi_{i\to j}\right)}{1 + \kappa_F {F_{i\to j}}^2} - \mu_F F_{i\to j}, \tag{2}$$

where $\phi_{i\to j}$ is the IAA flux across the interface, ρ_{F_0} controls the base rate of increase, ρ_F controls flux-based increase, κ_F is a limiting coefficient, and μ_F controls the rate of decay.

We define a variable z_i that controls the transition from PIN1 allocation based on IAA concentration to allocation based on IAA flux:

$$z_i = \min\left(\frac{IAA_i}{S_{PIN}}, 1.0\right). \tag{3}$$

As the IAA concentration in cell *i* increases from 0 to the threshold concentration S_{PIN}, z_i increases linearly from 0 to 1. S_{PIN} is given as a model parameter. We now define variables $Z_{i\to j}$ that are used to compute the overall allocation of PIN1 to membrane sections:

$$Z_{i\to j} = L_D + \left(1.0 - z_i\right) L_C IAA_j + z_i L_F F_{i\to j}. \tag{4}$$

L_D is a parameter controlling auxin-independent PIN allocation, L_C controls allocation based on concentration, and L_F controls allocation based on flux. PIN1 is allocated to cell membrane sections at each time step as follows:

$$PIN_{i\to j} = PIN_i \frac{B_{(i,j)} \cdot l_{i\to j} {b_{PIN}}^{Z_{i\to j}}}{\sum_{k\in N_i} B_{(i,k)} \cdot l_{i\to k} {b_{PIN}}^{Z_{i\to k}}} \tag{5}$$

where $k \in N_i$ are the neighbors of cell *i*, $PIN_{i\to j}$ represents the amount of PIN1 in cell *i* allocated to the section of the plasma membrane facing cell *j*, $l_{i\to j}$ is the length of the interface, and b_{PIN}, given as a model parameter, is the base for exponential PIN1 allocation. The equation controlling IAA concentration in a cell can now be written as:

$$\frac{d\,IAA_i}{dt} = \frac{\rho_{IAA}}{1+\kappa_{IAA}IAA_i} - \mu_{IAA}IAA_i - \frac{D_{IAA}}{A_i}\sum_{j\in N_i} B_{(i,j)}\cdot l_{i\to j}\left(IAA_i - IAA_j\right) - \frac{T_{IAA}}{A_i}\sum_{j\in N_i} B_{(i,j)}\left(PIN_{i\to j}\frac{IAA_i^{\,2}}{1+\kappa_T IAA_j^{\,2}} - PIN_{j\to i}\frac{IAA_j^{\,2}}{1+\kappa_T IAA_i^{\,2}}\right) \quad (6)$$

where ρ_{IAA} controls IAA production, κ_{IAA} is the production limiting coefficient, μ_{IAA} controls IAA decay, D_{IAA} is the diffusion coefficient, T_{IAA} controls transport, κ_T is the transport limiting coefficient, and A_i is the area of the polygon representing cell *i*.

Implementation of tissue polarity

The requirement for high concentration of auxin as the midvein is initiating creates a difficulty if the mechanism is also supposed to make the initiating vein follow a relatively shallow gradient of auxin in order to find existing vasculature. In the noisy environment of irregularly shaped cells, one would expect that any shallow gradient of auxin towards a sink would only be able to influence vein propagation in close proximity to that sink. This suggests that something else is likely involved in directing the vein. This additional signal can be incorporated into the model geometrically, as a simple rule, so that the sections of the plasma membrane that are closer to the existing vasculature would receive proportionally more flux-based allocation of PIN1 than the sections that are farther away. Alternatively, the signal can be implemented as a substance that is produced by the existing vasculature and diffuses throughout the meristem creating a gradient. Similar results were obtained in both cases, so we present the model based on a diffusing signaling substance.

The change in concentration of this vein attraction factor *VAF* in cell *i* is given by:

$$\frac{d\,VAF_i}{dt} = \frac{\rho_{VAF}}{1+\kappa_{VAF}VAF_i} - \mu_{VAF}VAF_i - \frac{D_{VAF}}{A_i}\sum_{j\in N_i} l_{i\to j}(VAF_i - VAF_j) \quad (7)$$

where ρ_{VAF} controls production, κ_{VAF} is a production limiting coefficient, μ_{VAF} controls decay, and D_{VAF} is the diffusion coefficient. ρ_{VAF} is zero everywhere except in older, differentiated vein cells where the attraction factor is produced.

Since the gradient of *VAF* will be quite shallow some distance from the source cells, an equation of a similar form as for PIN1 allocation is used to respond to the *VAF* concentration in neighbor cells. For each section of cell membrane in cell *i* facing cell *j* we calculate the value:

$$V_{i\to j} = \frac{l_{i\to j}(b_{VAF}{}^{VAF_j} - 1)}{\sum_{k\in N} l_{i\to k}(b_{VAF}{}^{VAF_k} - 1)} \tag{8}$$

where b_{VAF} is the base for exponential *VAF* allocation. $V_{i\to j}$ is then used to influence the

flux-based term in equation (4) as follows:

$$Z_{i\to j} = \left(L_D + (1.0 - z_i)L_C IAA_j + z_i L_F V_{i\to j} F_{i\to j}\right) \tag{9}$$

Model parameters

Where data were available, model parameters have been chosen to be compatible with measured values. In some cases this is straightforward, such as for cell sizes in the cellular template model, which have been taken directly from a tomato meristem section. Similarly, parameters have been chosen so that midvein initiation takes approximately 6-12 hours, consistent with our experimental observation. Although there is some published quantitative data for auxin diffusion and transport (see Swarup *et al*. (Swarup et al. 2005) for a review), this data only translates directly into parameter values for implementations of the chemiosmotic model of auxin transport that include extra-cellular space (Goldsmith et al. 1981; Kramer 2004; Swarup et al. 2005; Heisler and Jonsson 2006; Jonsson et al. 2006; Grieneisen et al. 2007). Nevertheless, Mitchison (Mitchison 1980a) showed that under suitable assumptions for diffusion of auxin through the cell's interior and apoplast, this data can still be meaningful in models that use a discretization of one compartment per cell. For this reason, we represent auxin concentration and parameters related to auxin synthesis, degradation, and passive and active transport, in real units. Maximum auxin levels attained in the simulations are in the range of 2-5 μM, which seems plausible based on experimental data (Uggla et al. 1996; Ljung et al. 2001; Wang et al. 2005). However, it is important not to attach too much significance to the auxin concentration values resulting in the model simulations, as these values can be changed considerably by adjusting model parameters. What is important is that the results can be obtained within reasonable values for auxin concentration and auxin-related parameters.

For the remaining parameters very little, if any, quantitative data are known. In this case we express concentration values and model parameters in abstract units. Note however, that the levels of PIN1 at cell membrane sections directly affect the rate of auxin transport. We therefore choose PIN1-related parameters (and VAF-related parameters in the cellular template model) such that membrane sections in the model where the maximum transport rate occurs have approximately one abstract unit of PIN1 per μm of

cell membrane section. This allows a straightforward comparison of the model's transport-related parameters with experimentally-based estimates of maximum auxin transport rates. Parameter values for the simulations are given in Table S1.

Table S1. Simulation parameters.

Parameter	Variable	Equations	Fig. 4	Fig. 7, 9A	Fig. 9C	Fig. 9B	Units
Integration time step	dt	1,2,6,7	.001	.001	.001	.001	hours
Cell wall length	l	5-8	10	5.4†	5.4†	5.4†	μm
Cell area	A	6,7	100	63.4†	63.4†	63.4†	μm^2
Boundary factor between L1 and inner tissue	B	2,5,6	.6	.5	.5	.5	
Auxin independent PIN1 production (L1 cells)	ρ_{PIN_0}	1	1	.3	.3	.3	
Auxin independent PIN1 production (inner tissue)	ρ_{PIN_0}	0	0	0	0	0	
PIN1 production (L1 cells)	ρ_{PIN}	1	1	.3	.3	.3	
PIN1 production (inner tissue)	ρ_{PIN}	1	2	.45	.45	.45	
PIN1 production limiting coefficient	κ_{PIN}	1	1	1	1	1	
PIN1 decay	μ_{PIN}	1	1	.05	.05	.05	
Flux history flux independent production	ρ_{F_0}	2	.01	.01	.01	.01	
Flux history production	ρ_F	2	.2	.2	.2	.2	
Flux history limiting coefficient	κ_F	2	50	50	50	50	
Flux history decay	μ_F	2	.1	.1	.1	.1	
IAA transition threshold, concentration to flux-based allocation (L1 cells)	S_{PIN}	3	4	4	4	4	μM
IAA transition threshold, concentration to flux-based allocation (inner tissue)	S_{PIN}	3	4	3	3	3	μM
PIN1 default allocation	L_D	4,9	0	1	1	1	
PIN1 concentration-based allocation	L_C	4,9	6	5	5	5	
PIN1 flux-based allocation	L_F	4,9	3	8	8	8	
Base for exponential PIN1 allocation	b_{PIN}	5	3	3	3	3	
IAA production (L1 cells)	ρ_{IAA}	6	4.5	.1	1.5	.1	$\mu mol\ l^{-1}\ hr^{-1}$
IAA production (L1 cells near primordium)‡	ρ_{IAA}	6		10	0	10	$\mu mol\ l^{-1}\ hr^{-1}$
IAA production (inner tissue)	ρ_{IAA}	6	0	0	0	0	$\mu mol\ l^{-1}\ hr^{-1}$
IAA production limiting coefficient	κ_{IAA}	6	1	1	1	1	
IAA decay	μ_{IAA}	6	.1	.1	.1	.1	hr^{-1}
IAA diffusion (L1 cells)	D_{IAA}	6	.006	.006	.006	.006	$cm\ hr^{-1}$
IAA diffusion (inner tissue)	D_{IAA}	6	.002	.002	.002	.002	$cm\ hr^{-1}$

IAA transport	T_{IAA}	6	.04	.1	.01	.04	cm hr^{-1}
VAF production	ρ_{VAF}	7		10	10	10	
VAF production limiting coefficient	κ_{VAF}	7		1	1	1	
VAF decay	μ_{VAF}	7		.1	.1	.1	
VAF diffusion	D_{VAF}	7		1	1	1	
Base for exponential VAF allocation	b_{VAF}	8		5	5	5	

†In the cellular template model, cell sizes are based on the meristem from which the template was derived. In this case the numbers above represent the averages of the cell area and cell wall length.
‡In the cellular template simulations, most of the IAA production occurs in an 8 cell region in the top right of the meristem. This production is in addition to a small amount of production in all of the L1 cells.

The model is robust with respect to parameter values, and most parameters can be varied considerably without qualitatively affecting the simulation results. Although an analytical solution for our model equations is likely not possible, it is possible to do some simple consistency checks (Kramer 2008). Data variables for the concentrations of biochemical substances and allocated quantities in the model are checked at each time step for out-of-range values (such as negative values for concentrations). In addition, all simulations have been repeated with several time steps, up to an order of magnitude smaller, yielding the same results.

REFERENCES

Bainbridge, K., S. Guyomarc'h, E. Bayer, R. Swarup, M. Bennett, T. Mandel, and C. Kuhlemeier. 2008. Auxin influx carriers stabilize phyllotactic patterning. *Genes & Development* **22**: 810-823.

Benkova, E., M. Michniewicz, M. Sauer, T. Teichmann, D. Seifertova, G. Jurgens, and J. Friml. 2003. Local, efflux-dependent auxin gradients as a common module for plant organ formation. *Cell* **115**: 591-602.

de Reuille, P.B., I. Bohn-Courseau, K. Ljung, H. Morin, N. Carraro, C. Godin, and J. Traas. 2006. Computer simulations reveal properties of the cell-cell signaling network at the shoot apex in Arabidopsis. *Proceedings of the National Academy of Sciences of the United States of America* **103**: 1627-1632.

Feugier, F.G. and Y. Iwasa. 2006. How canalization can make loops: A new model of reticulated leaf vascular pattern formation. *Journal of Theoretical Biology* **243**: 235-244.

Feugier, F.G., A. Mochizuki, and Y. Iwasa. 2005. Self-organization of the vascular system in plant leaves: Inter-dependent dynamics of auxin flux and carrier proteins. *Journal of Theoretical Biology* **236**: 366-375.

Fleming, A.J., S. McQueenMason, T. Mandel, and C. Kuhlemeier. 1997. Induction of leaf primordia by the cell wall protein expansion. *Science* **276**: 1415-1418.

Goldsmith, M.H.M., T.H. Goldsmith, and M.H. Martin. 1981. Mathematical-Analysis of the Chemosmotic Polar Diffusion of Auxin through Plant-Tissues. *Proceedings of*

the National Academy of Sciences of the United States of America-Biological Sciences **78**: 976-980.
Grieneisen, V.A., J. Xu, A.F.M. Maree, P. Hogeweg, and B. Scheres. 2007. Auxin transport is sufficient to generate a maximum and gradient guiding root growth. *Nature* **449**: 1008-1013.
Heisler, M.G. and H. Jonsson. 2006. Modeling auxin transport and plant development. *Journal of Plant Growth Regulation* **25**: 302-312.
Heisler, M.G., C. Ohno, P. Das, P. Sieber, G.V. Reddy, J.A. Long, and E.M. Meyerowitz. 2005. Patterns of auxin transport and gene expression during primordium development revealed by live imaging of the Arabidopsis inflorescence meristem. *Current Biology* **15**: 1899-1911.
Jonsson, H., M.G. Heisler, B.E. Shapiro, E.M. Meyerowitz, and E. Mjolsness. 2006. An auxin-driven polarized transport model for phyllotaxis. *Proceedings of the National Academy of Sciences of the United States of America* **103**: 1633-1638.
Kramer, E.M. 2004. PIN and AUX/LAX proteins: their role in auxin accumulation. *Trends in Plant Science* **9**: 578-582.
-. 2006. How far can a molecule of weak acid travel in the apoplast or xylem? *Plant Physiology* **141**: 1233-1236.
-. 2008. Computer models of auxin transport: a review and commentary. *Journal of Experimental Botany* **59**: 45-53.
Ljung, K., R.P. Bhalerao, and G. Sandberg. 2001. Sites and homeostatic control of auxin biosynthesis in Arabidopsis during vegetative growth. *Plant Journal* **28**: 465-474.
Mitchison, G.J. 1980a. The Dynamics of Auxin Transport. *Proceedings of the Royal Society of London Series B-Biological Sciences* **209**: 489-511.
-. 1980b. Model for Vein Formation in Higher-Plants. *Proceedings of the Royal Society of London Series B-Biological Sciences* **207**: 79-109.
-. 1981. The Polar Transport of Auxin and Vein Patterns in Plants. *Philosophical Transactions of the Royal Society of London Series B-Biological Sciences* **295**: 461-&.
Reinhardt, D., T. Mandel, and C. Kuhlemeier. 2000. Auxin regulates the initiation and radial position of plant lateral organs. *Plant Cell* **12**: 507-518.
Reinhardt, D., F. Wittwer, T. Mandel, and C. Kuhlemeier. 1998. Localized upregulation of a new expansin gene predicts the site of leaf formation in the tomato meristem. *Plant Cell* **10**: 1427-1437.
Rolland-Lagan, A.G. and P. Prusinkiewicz. 2005. Reviewing models of auxin canalization in the context of leaf vein pattern formation in Arabidopsis. *Plant Journal* **44**: 854-865.
Smith, C., P. Prusinkiewicz, F. Samavati. 2003. Local specification of surface subdivision algorhithms. *Lecture Notes in Computer Science* **3062**: 313-327.
Smith, R.S., S. Guyomarc'h, T. Mandel, D. Reinhardt, C. Kuhlemeier, and P. Prusinkiewicz. 2006. A plausible model of phyllotaxis. *Proc Nat Acad Sci USA* **103**: 1301-1306.
Swarup, R., E.M. Kramer, P. Perry, K. Knox, H.M.O. Leyser, J. Haseloff, G.T.S. Beemster, R. Bhalerao, and M.J. Bennett. 2005. Root gravitropism requires lateral root cap and epidermal cells for transport and response to a mobile auxin signal. *Nature Cell Biology* **7**: 1057-1065.

Uggla, C., T. Moritz, G. Sandberg, and B. Sundberg. 1996. Auxin as a positional signal in pattern formation in plants. *Proceedings of the National Academy of Sciences of the United States of America* **93**: 9282-9286.

Wang, S.C., S.B. Tiwari, G. Hagen, and T.J. Guilfoyle. 2005. AUXIN RESPONSE FACTOR7 restores the expression of auxin-responsive genes in mutant Arabidopsis leaf mesophyll protoplasts. *Plant Cell* **17**: 1979-1993.

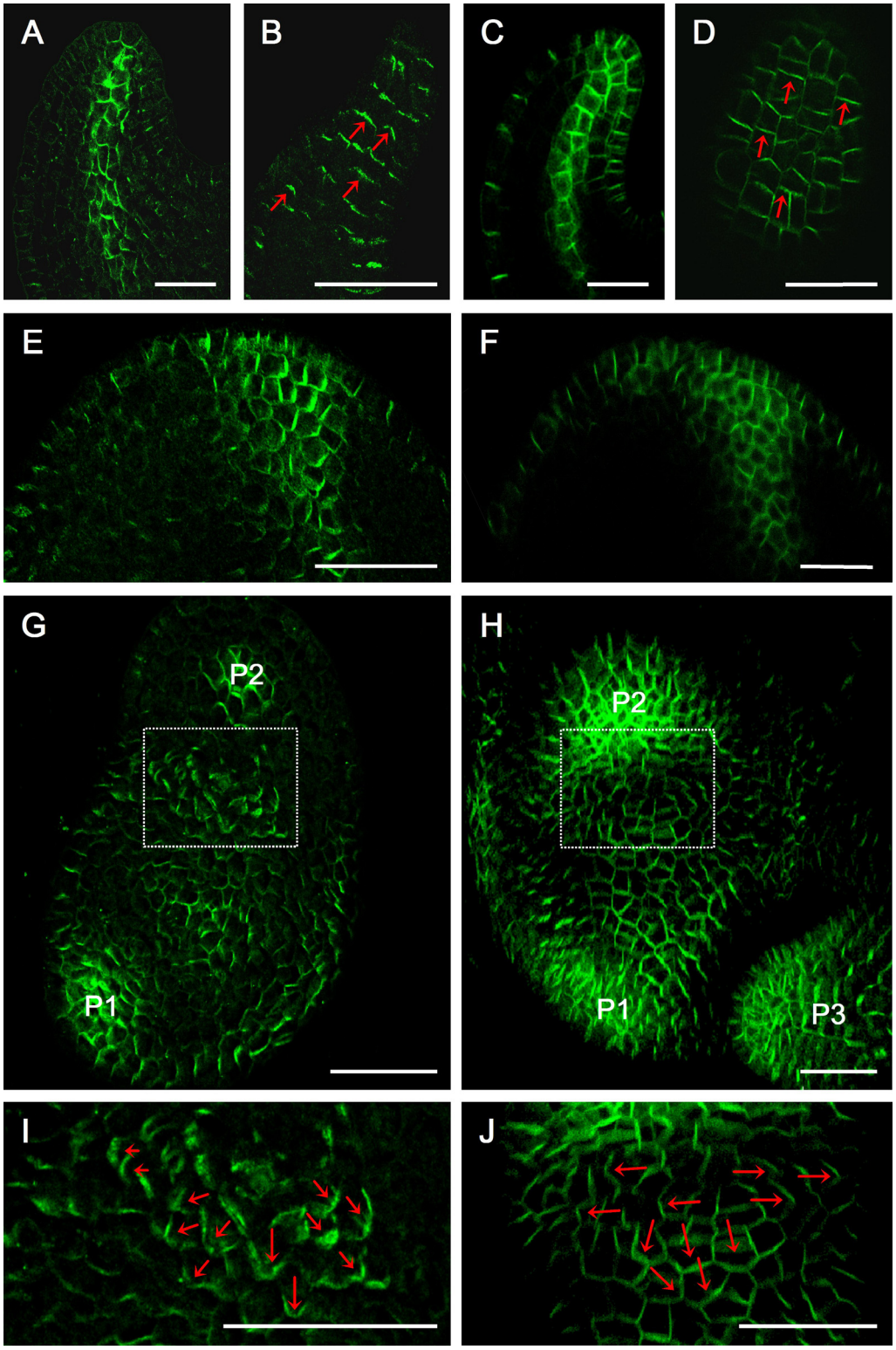

Figure S1. Comparison between tomato PIN1 and Arabidopsis PIN1:GFP expression pattern in tomato vegetative shoot apices. Tomato PIN1 and Arabidopsis PIN1 displayed a highly similar expression profile in tomato shoot apices. (A-D) PIN1 expression in developping midvein (A and C) and epidermis (B and D) of young leaf

primordia. Red arrows indicates PIN1 polarity. (E, F) Longitudinal sections through incipient primordia showing PIN1 expression in a V-shaped domain extending into inner tissues. (G, H) Cross section views of tomato shoot apical meristem. P designates leaf primordia with P1 representing the youngest primordium. (I, J) Close up of the same sections as depicted in panels G and H respectively (white frames), showing PIN1 polarity (red arrows) at the boundary between leaf primordia and the meristem. (A, B, E, G, I) Tomato PIN1 protein. Immunolocalization on wax sections. (C, D, F, H, J) Arabidopsis PIN1:GFP fusion protein. Confocal optical sections. Scale bars, 40 µm.

Figure S2. Tomato PIN1 expression in the stem of tomato vegetative apices. Longitudinal section through a stem showing PIN1 expression in elongated parenchymatous xylem cells (left) and in epidermal cells (right). White arrow indicates PIN1 polarity. Scale bars, 25 µm.

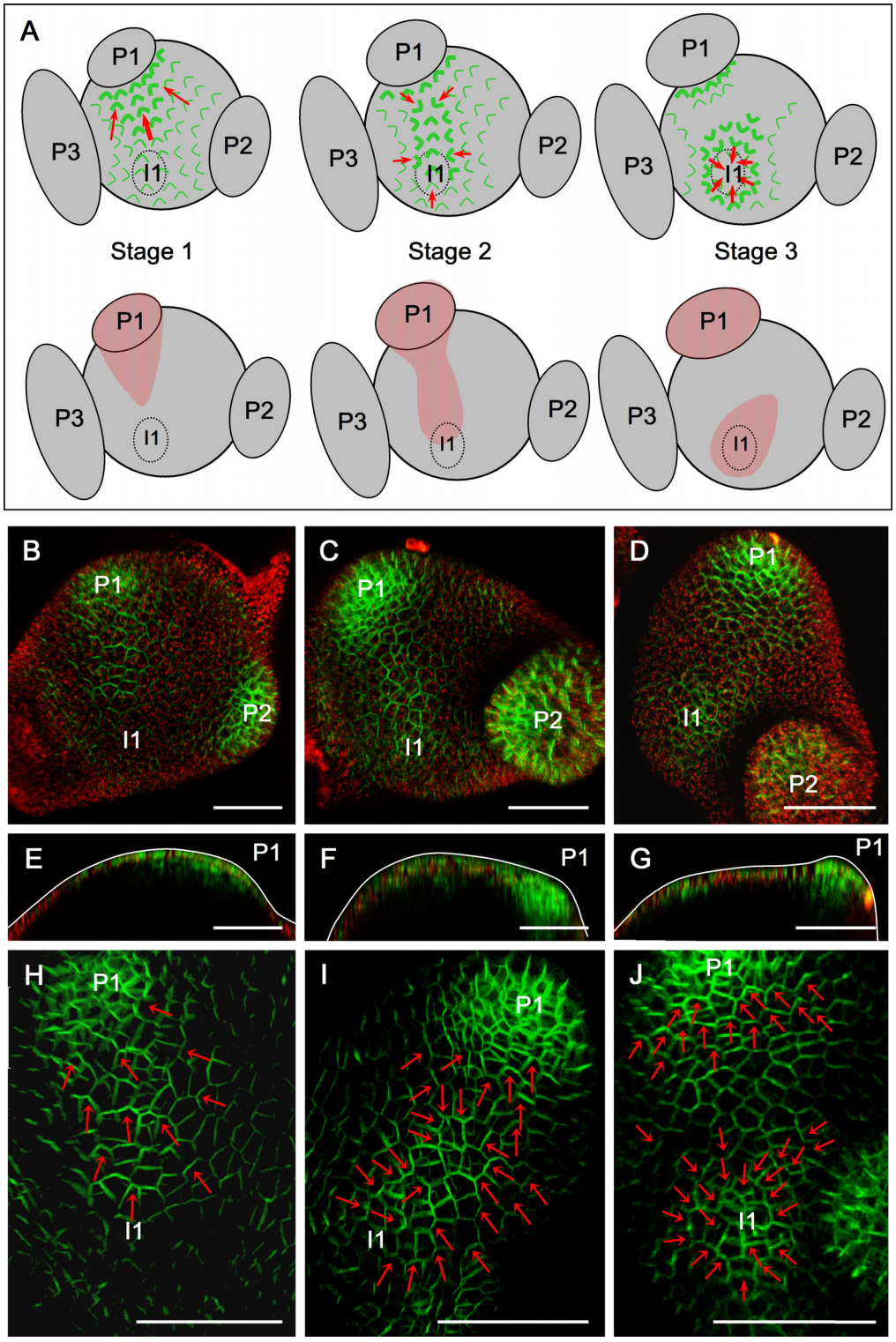

Figure S3. Formation of PIN1 convergence point at the incipient leaf primordium in the L1 of tomato meristem. Based on the analysis of a large sample of tomato meristems (n=52) expressing AtPIN1:GFP, we divided the establishment of a convergence point at I1, into three stages. First, an up-regulation of PIN1 expression was

observed in an elongated domain starting from P1 (the earliest bulging primordium) and extending towards the meristem centre (A, B and H). At this stage, overall PIN1 polarization in this domain was clearly directed towards P1 (H), which is just starting to bulge (E). At the meristem flanks, PIN1 was found to polarize away from adjacent older primordia, i.e. P2 and P3. At stage 2, PIN1 polarity gradually changed from being strictly directed towards P1 to become oriented laterally towards the meristem centre (A, C and I). At stage 3, PIN1 polarity had completely reversed, away from P1, and the formation of a closed, concentric convergence point at I1 was complete (A, D and J). Extending from I1 towards the meristem summit, a PIN1 expression domain with polarity directed towards I1 was very often observed at this stage (see Fig.1 E). Time lapse study revealed that the time between stage 1 and stage 3 was approximately 24h (data not shown). Moreover, although stages 1 and 3 could easily be observed, representing each 40% of the total number of observed meristem (n=52), stage 2 was more difficult to capture (20% of the total number of observed meristem). We therefore deduced that stage 2 is a relatively fast event when compare to stages 1 and 3.

(A) Schematic representation of the three stages of I1 specification. (Top row) AtPIN1:GFP polarization and expression pattern. AtPIN1:GFP is represented by green arcs and the deduced overall auxin direction is represented by red arrows. Areas of higher AtPIN1:GFP expression are indicated by thicker green arcs. (Second row) Overall auxin distribution (red) as predicted by AtPIN1:GFP expression pattern and polarization in corresponding top row. (B-D) 3D reconstruction of vegetative tomato meristems viewed from above, illustrating the three consecutive stages of I1 specification as in panel A. Green signal is AtPIN1:GFP protein and red signal is plastids autofluorescence. (E-G) Reconstructed longitudinal sections through P1 of meristems showed in B, C and D respectively. (H-J) Closer views of regions surrounding P1 and I1 of the same meristems as depicted in panels B, C and D respectively. AtPIN1:GFP polarization is indicated by red arrows. P designates bulging leaf primordia with P1 representing the youngest primordium. I1 designates incipient primordium. Scale bars, 60 μm.

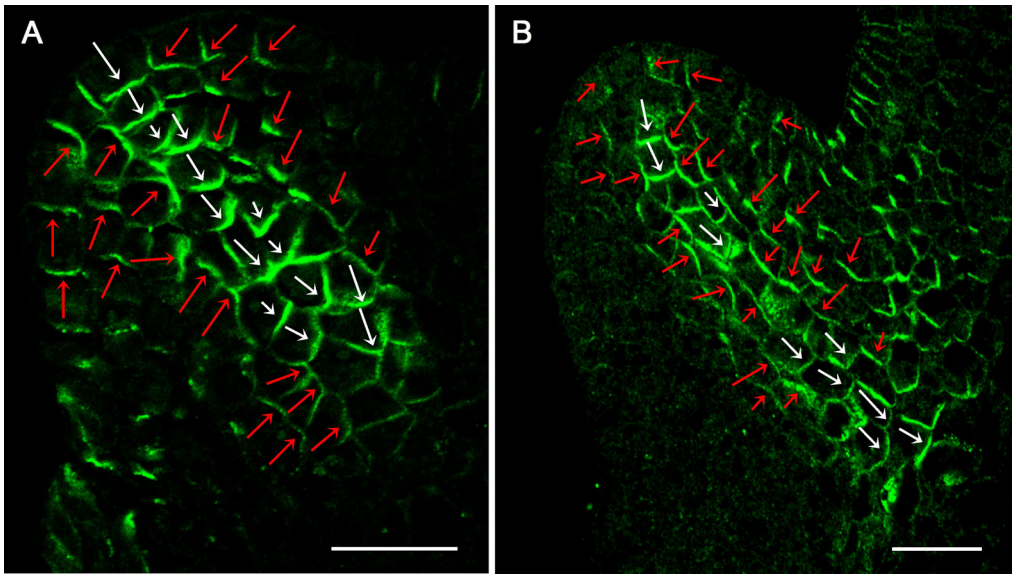

Figure S4. Basal and lateral PIN1 polarization in initiating midvein of sepal and leaflet primordia. Tomato PIN1 immunolocalization, visualized by confocal imaging. Longitudinal median sections through a bulging sepal primordia (A) and leaflet primordia (B). PIN1 polarization is indicated by arrows (red for lateral towards the future midvein and white for basal). Scale bars, 20 µm.

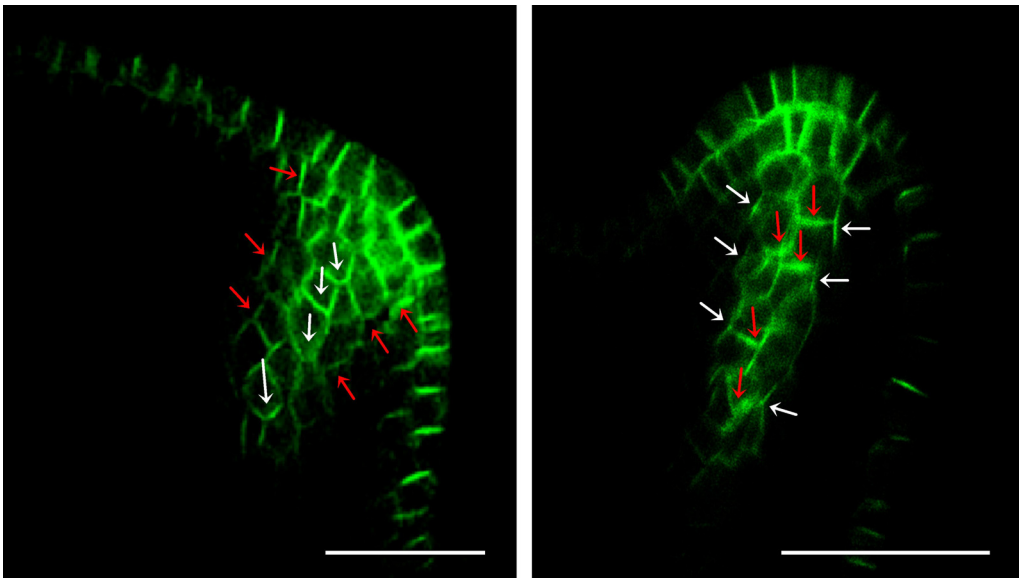

Figure S5. Basal and lateral AtPIN1:GFP polarization in initiating leaf midvein. Longitudinal optical sections through leaf primordia of a trangenic tomato plant. Red arrows, lateral; white arrows, basal polarization. Scale bar, 50 µm.

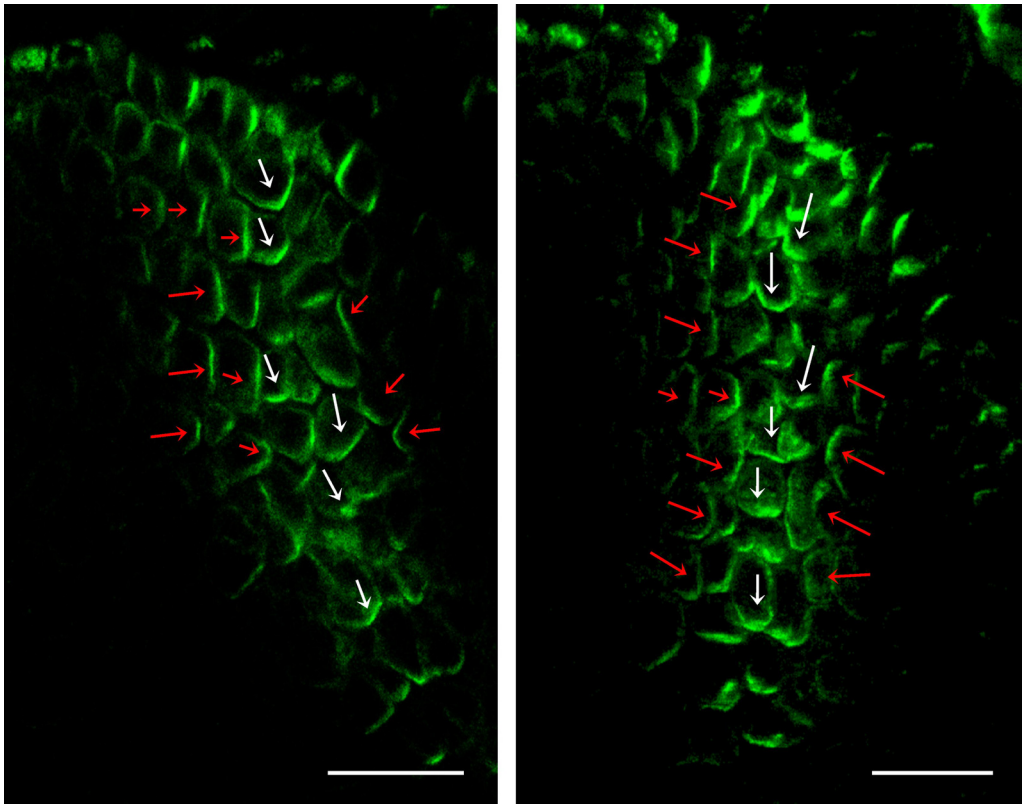

Figure S6. Basal and lateral PIN1 polarization in initiating leaf midvein in Arabidopsis. Arabidopsis PIN1 immunolocalization, visualized by confocal imaging. Longitudinal median sections through initiating leaf midvein. PIN1 polarization is indicated by arrows (red for lateral towards the future midvein and white for basal). Scale bars, 20 µm.

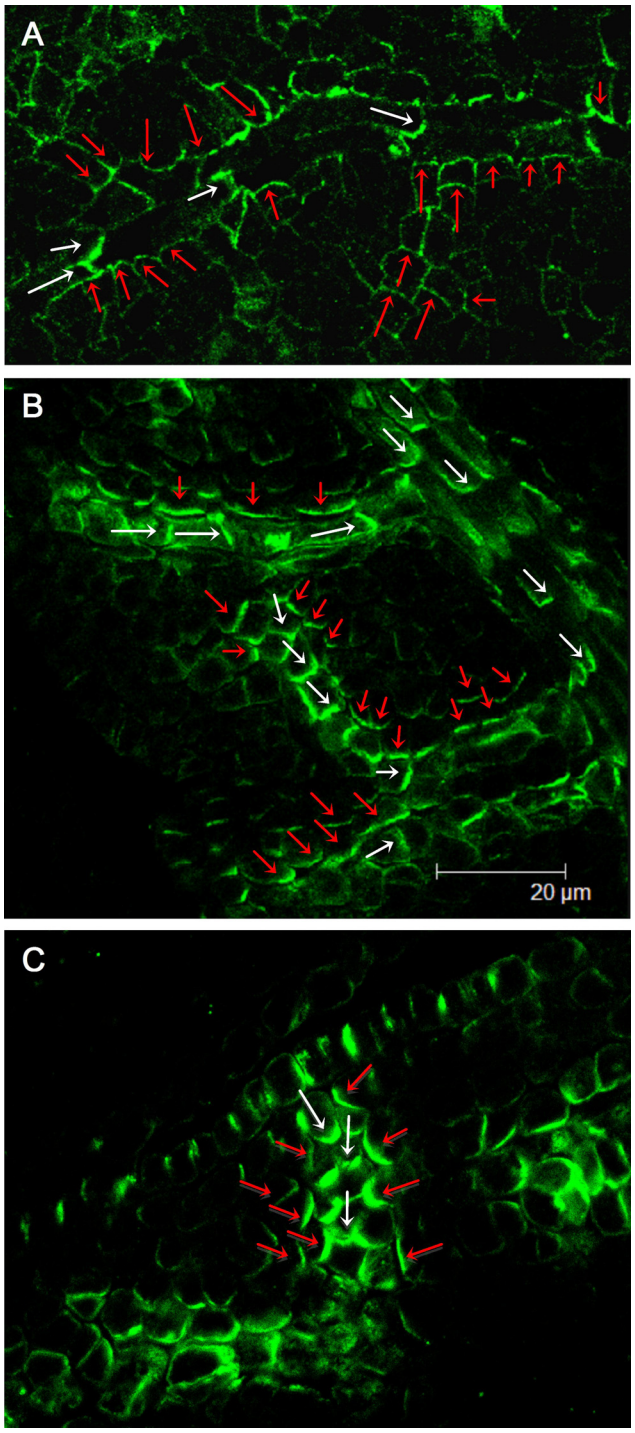

Figure S7. PIN1 lateral polarization towards developping higher order leaf veins. PIN1 immunolocalization visualized by confocal imaging. Longitudinal median sections through second and third order leaf veins of tomato (A) and Arabidopsis (B, C). Note PIN1 polarization perpendicular to the developping veins in surrounding cells (red arrows). Scale bars, 20 µm.

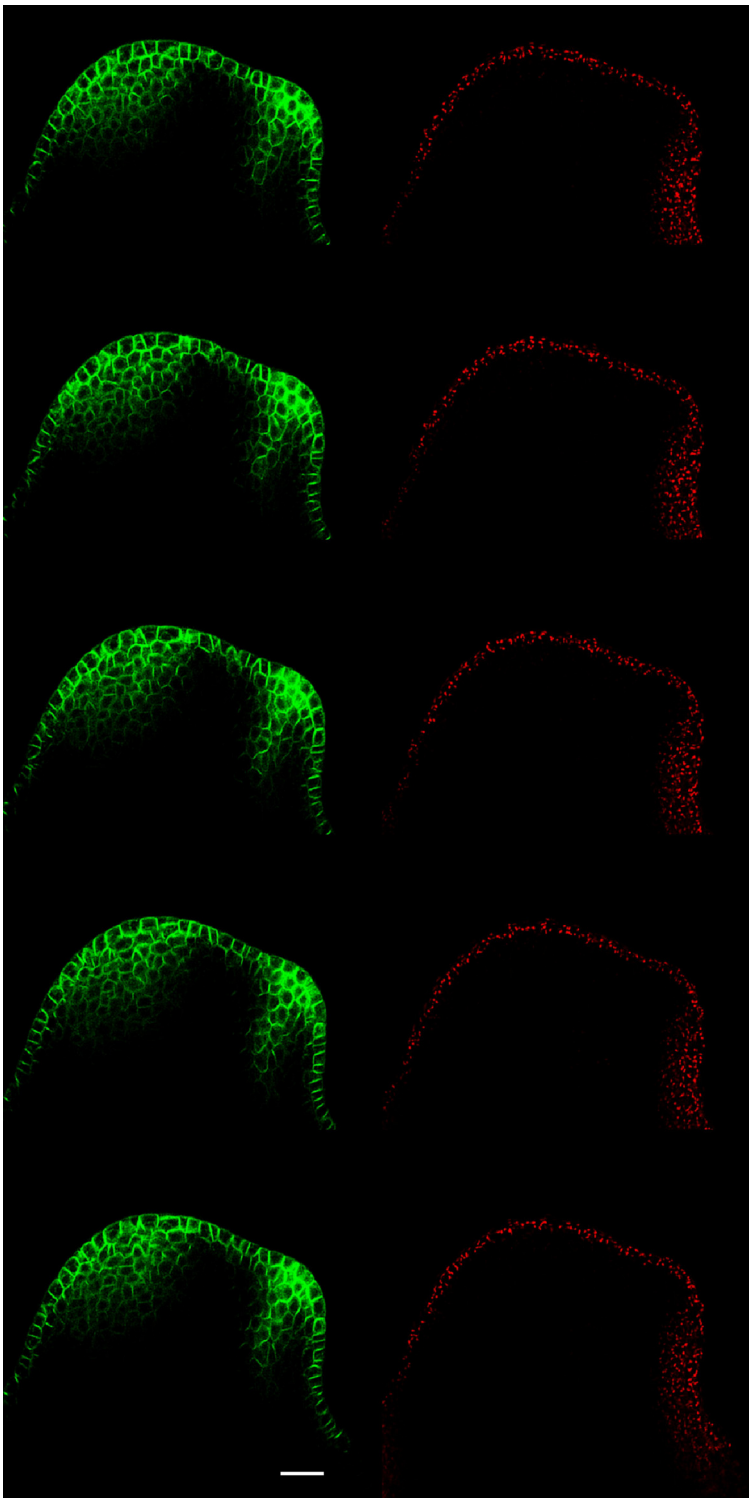

Figure S8. Consecutive longitudinal confocal sections through I1 and P1 of wild type tomato vegetative meristem expressing AtPIN1:GFP. Same meristem as in Fig. 5A. Green signal is AtPIN1:GFP protein and red signal is plastid autofluorescence. Note that at the meristem red plastid autofluorescence signal is restricted to the L1 layer only. Scale bars, 20µm.

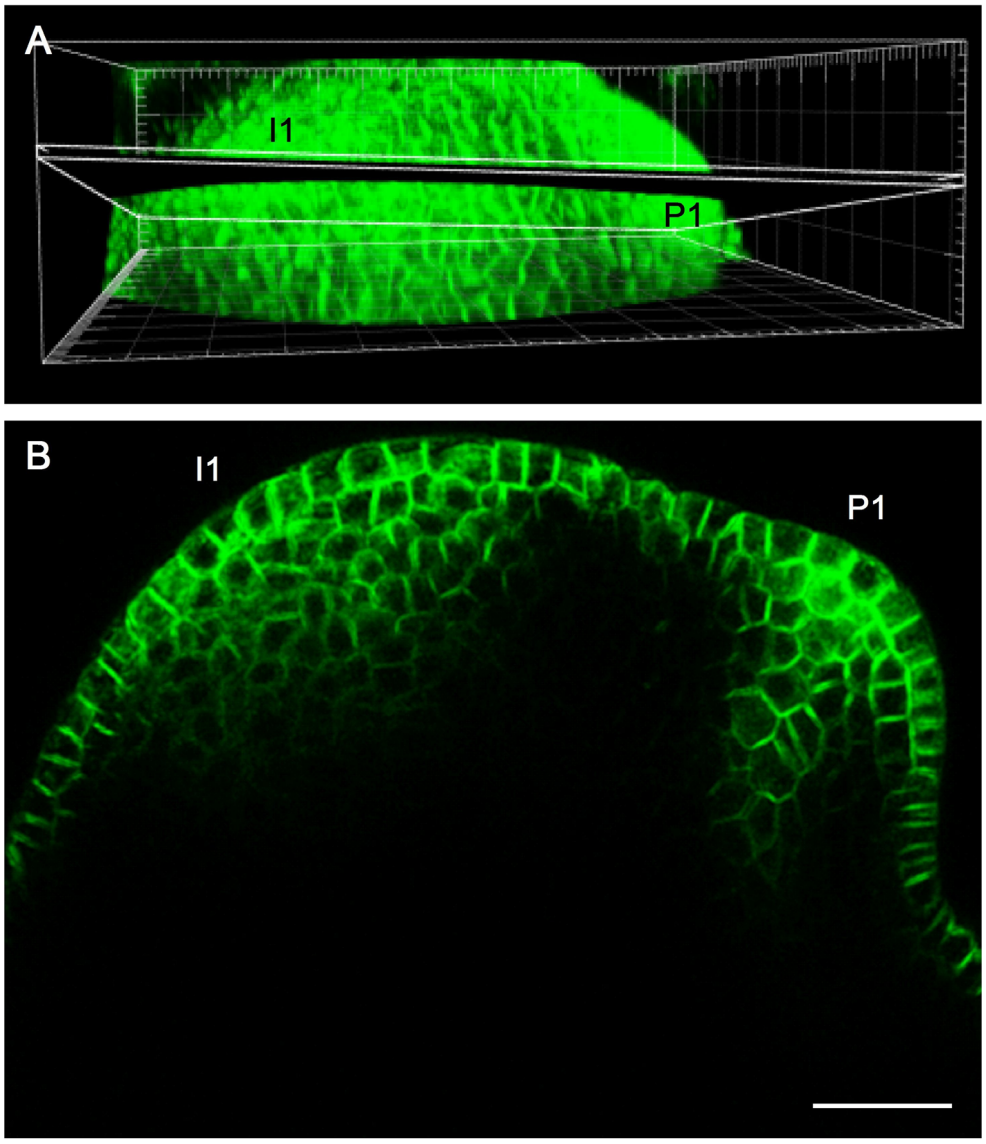

Figure S9. Reconstructed longitudinal section through I1 and P1 of wild type tomato vegetative meristem expressing AtPIN1:GFP. (A) 3D reconstruction of the same vegetative tomato meristem as in Fig. 5A, viewed from above. The white frame indicates the position of the longitudinal section plane viewed in panel B. (B) Reconstructed longitudinal section (4 µm) I1 and P1 as shown in A. Scale bar, 20µm.

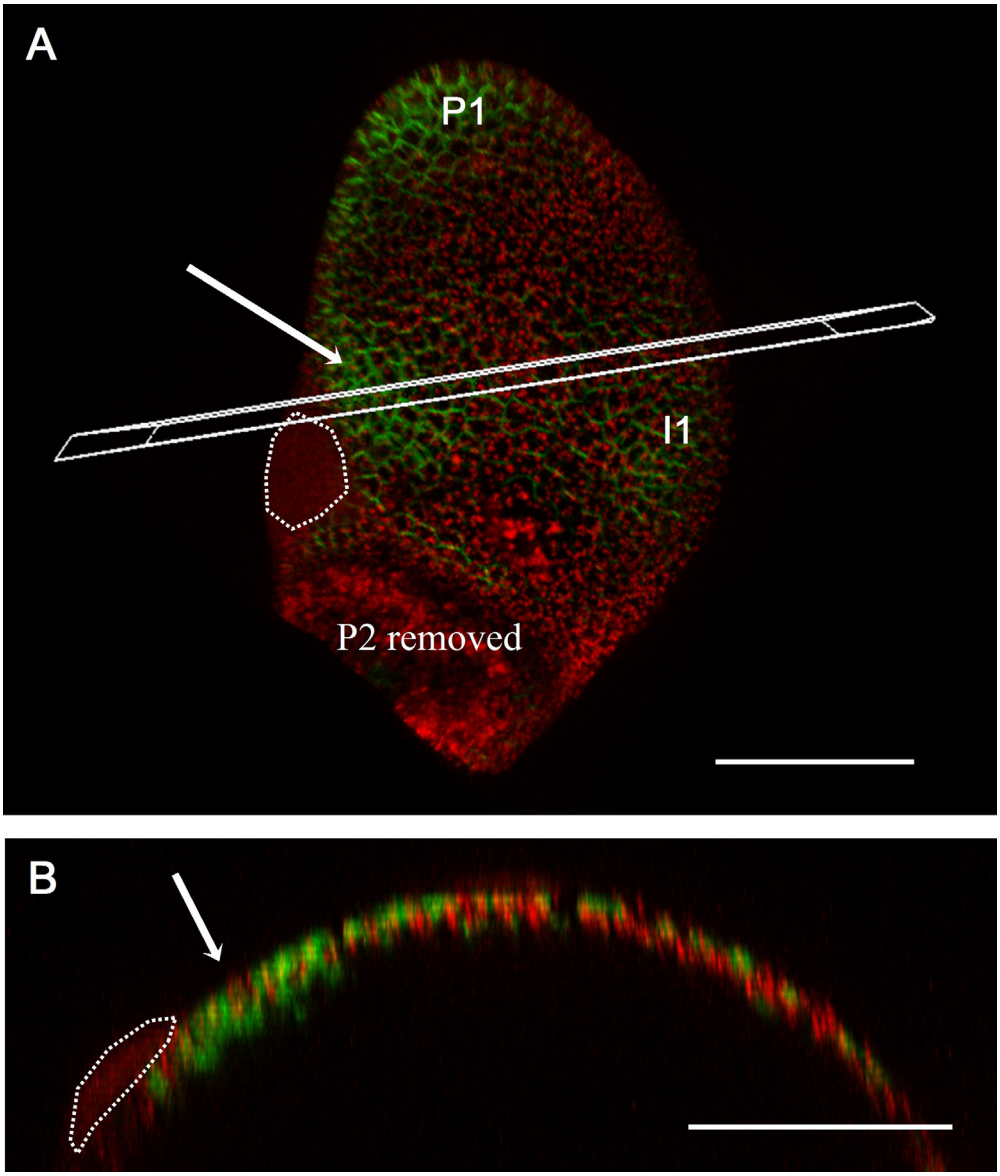

Figure S10. Reconstructed longitudinal section through a convergence point at I2 induced by IAA application. (A) 3D reconstruction of the same vegetative tomato meristem as in Fig. 6B after 20h IAA-microapplication at I2. The white frame indicates the position of the longitudinal section plane viewed in panel B. (B) Reconstructed longitudinal section (8 µm) through auxin-induced PIN1 convergence point as shown in A. Note that no bulging is yet visible at I2. White arrow indicates the position of auxin-induced PIN1 convergence point. White dotted lines indicates IAA-containing lanolin that has sliden down. Scale bars, 50µm.

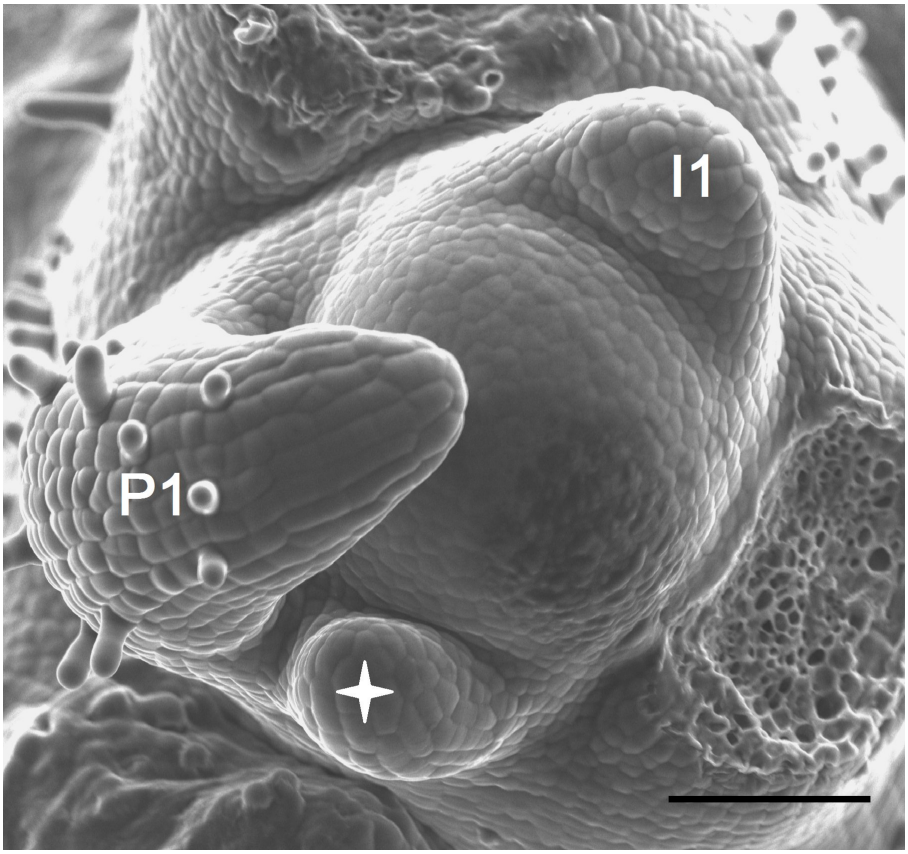

Fig. S11. **Induction of an aberrantly positioned leaf primordium by application of exogenous IAA.** The angle between I1 and the induced primordium (white star) is close to 180° rather than the golden angle of 137.5°. Scale bar, 50 μm.

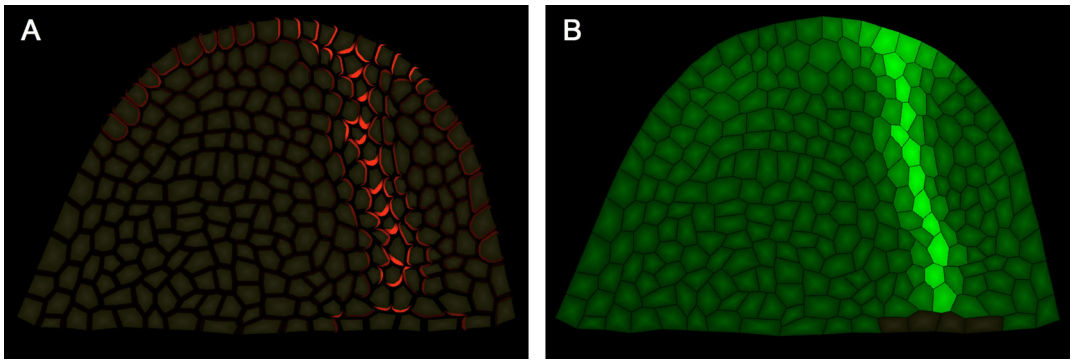

Fig. S12. **Simulation of midvein formation using a geometric rule for the vein attraction factor**. A) PIN localization within cells shown in red. B) Auxin levels shown in green. Dark cells in the bottom right represent pre-existing vasculature. The geometric rule produces similar results to the model that assumes a diffusing substance. Compare with figure Fig. 7 (E,F).

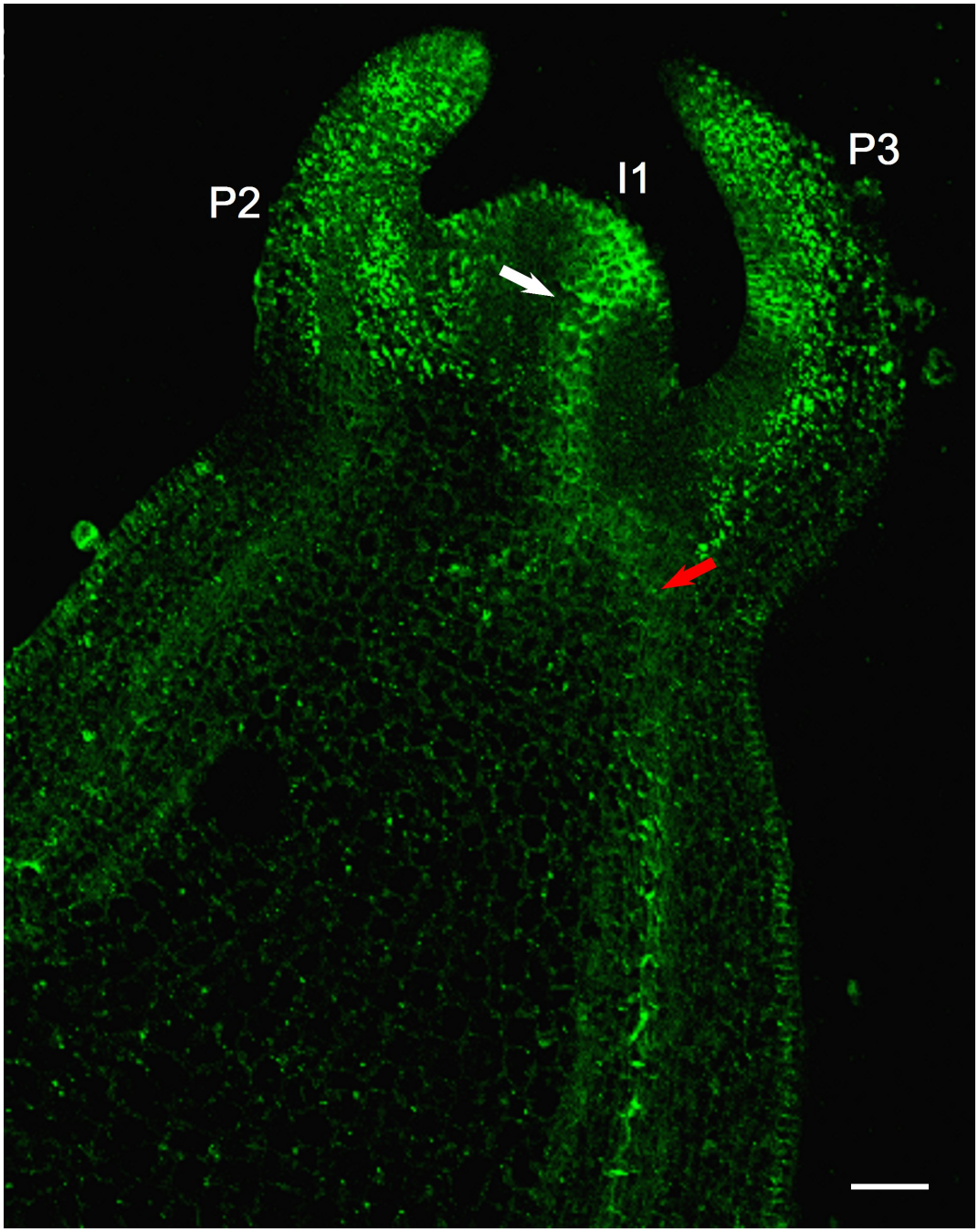

Fig. S13. **I1 midvein connection to P3 vasculature.** Tomato PIN1 immunolocalization, visualized by confocal imaging. Longitudinal median section through initiating I1 midvein of wild type tomato apex. Note the connection of I1 midvein (white arrow) to P3 vasculature (red arrow). Scale bar, 50 μm.

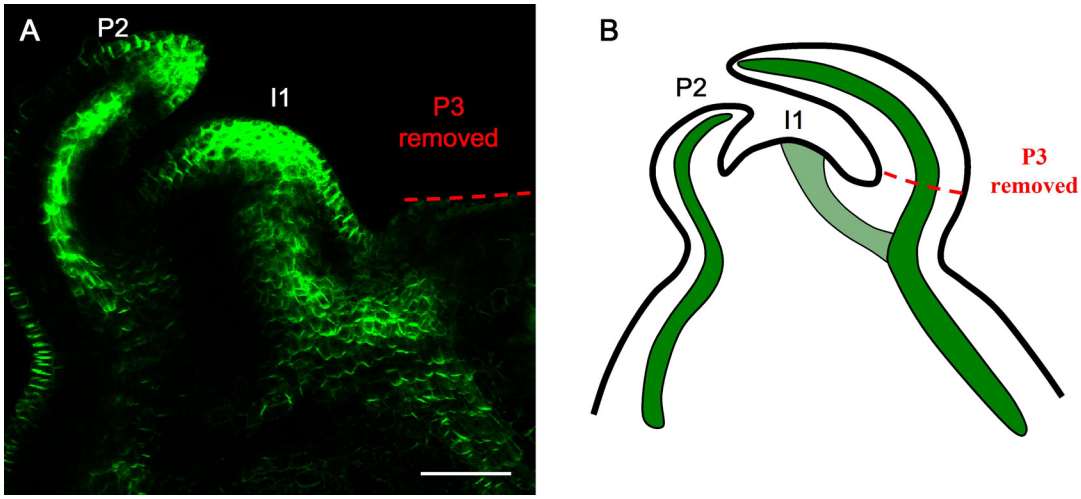

Fig. S14. (A) Control meristem showing the initiating midvein at I1 connecting to P3 vein. See also Fig. 8. As a control for wounding effects, P3 was removed (red dashed line) but the section of P3 vasculature to which I1 midvein connects to was left intact. Maximal projection of longitudinal confocal scans of wild-type tomato meristems expressing AtPIN1:GFP. (B) Schematic representations of (A). P designates bulging leaf primordia with P1 representing the youngest primordium. I1 designates incipient primordium. Scale bars, 50 µm.

MOVIE CAPTIONS

Movie S1. Model of midvein formation on a rectangular grid of cells. This is an animation of the same simulation shown in Fig. 4 in the main text. Auxin concentration is shown in blue, PIN1 allocation in red. Length and width of arrows indicate the magnitude and dominant direction of auxin flux. Auxin is supplied to the top row of cells that represent the L1 layer (outlined in green) in the meristem. A single sink cell in the middle of the last row (outlined in red) represents the existing vasculature of the plant, simulated by an increased rate of IAA decay**.** Initially, cells in the L1 layer self-organize to specify the site of organ primordium initiation by creating a local auxin maximum, with PIN1 in neighboring cells oriented towards this convergence point. As auxin levels increase, up-the-gradient allocation transitions to with-the-flux allocation, and the convergence point begins to extend into inner tissue. As the simulation proceeds, the vein continues to extend until it connects to the existing vasculature. Total simulation time represents 16 hours.

Movie S2. Simulation model of midvein formation on a cellular meristem template. This is an animation of the same simulation shown in Fig. 7 in the main text. PIN1 protein localization shown in red (left), and IAA concentration shown in green (right). Dark cells at the bottom right are sinks for auxin and represent pre-existing vasculature. Total simulation time represents 14 hours.